

Deep Photometric Observations of Ultrafaint Milky Way Satellites Centaurus I and Eridanus IV*

Quinn O. Casey¹, Burçin Mutlu-Pakdil¹, David J. Sand², Andrew B. Pace³, Denija Crnojević⁴,
 Amandine Doliva-Dolinsky¹, William Cerny⁵, Mairead E. Heiger^{6,7}, Alex H. Riley⁸, Alexander P. Ji^{9,10},
 Guilherme Limberg^{10,11}, Laurella Marin¹, Clara E. Martínez-Vázquez¹², Gustavo E. Medina⁶, Ting S. Li⁶,
 Sasha N. Campana¹, Astha Chaturvedi¹³, Joanna D. Sakowska¹³, Alfredo Zenteno¹⁴, Julio A. Carballo-Bello¹⁵,
 Mahdieh Navabi¹³, Clecio R. Bom¹⁶, and (DELVE Collaboration)

¹ Department of Physics and Astronomy, Dartmouth College, Hanover, NH 03755, USA; quinn.o.casey.gr@dartmouth.edu

² Steward Observatory, University of Arizona, 933 North Cherry Avenue, Tucson, AZ 85721-0065, USA

³ Department of Astronomy, University of Virginia, 530 McCormick Road, Charlottesville, VA 22904, USA

⁴ Department of Physics and Astronomy, University of Tampa, 401 West Kennedy Boulevard, Tampa, FL 33606, USA

⁵ Department of Astronomy, Yale University, New Haven, CT 06520, USA

⁶ Department of Astronomy and Astrophysics, University of Toronto, 50 St George Street, Toronto, ON M5S 3H4, Canada

⁷ Dunlap Institute for Astronomy and Astrophysics, University of Toronto, 50 St George Street, Toronto, ON M5S 3H4, Canada

⁸ Institute for Computational Cosmology, Department of Physics, Durham University, South Road, Durham DH1 3LE, UK

⁹ Department of Astronomy & Astrophysics, University of Chicago, 5640 S. Ellis Avenue, Chicago, IL 60637, USA

¹⁰ Kavli Institute for Cosmological Physics, University of Chicago, Chicago, IL 60637, USA

¹¹ Universidade de São Paulo, IAG, Departamento de Astronomia, SP 05508-090, São Paulo, Brazil

¹² International Gemini Observatory/NSF NOIRLab, 670 N. A'ohoku Place, Hilo, HI 96720, USA

¹³ Department of Physics, University of Surrey, Guildford GU2 7XH, UK

¹⁴ Cerro Tololo Inter-American Observatory/NSF NOIRLab, Casilla 603, La Serena, Chile

¹⁵ Instituto de Alta Investigación, Universidad de Tarapacá, Casilla 7D, Arica, Chile

¹⁶ Centro Brasileiro de Pesquisas Físicas, Rua Dr. Xavier Sigaud 150, 22290-180 Rio de Janeiro, RJ, Brazil

Received 2025 January 8; revised 2025 March 17; accepted 2025 March 17; published 2025 May 7

Abstract

We present deep Magellan+Megacam imaging of Centaurus I (Cen I) and Eridanus IV (Eri IV), two recently discovered Milky Way ultrafaint satellites. Our data reach $\sim 2\text{--}3$ mag deeper than the discovery data from the DECam Local Volume Exploration Survey. We use these data to constrain their distances, structural properties (e.g., half-light radii, ellipticity, and position angle), and luminosities. We investigate whether these systems show signs of tidal disturbance and identify new potential member stars using Gaia EDR3. Our deep color–magnitude diagrams show that Cen I and Eri IV are consistent with an old ($\tau \sim 13.0$ Gyr) and metal-poor ($[\text{Fe}/\text{H}] \leq -2.2$) stellar population. We find Cen I to have a half-light radius of $r_h = 2'.60 \pm 0'.30$ (90.6 ± 11 pc), an ellipticity of $\epsilon = 0.36 \pm 0.05$, a distance of $D = 119.8 \pm 4.1$ kpc ($m - M = 20.39 \pm 0.08$ mag), and an absolute magnitude of $M_V = -5.39 \pm 0.19$. Similarly, Eri IV has $r_h = 3'.24 \pm 0'.48$ (65.9 ± 10 pc), $\epsilon = 0.26 \pm 0.09$, $D = 69.9 \pm 3.6$ kpc ($m - M = 19.22 \pm 0.11$ mag), and $M_V = -3.55 \pm 0.24$. These systems occupy a space on the size–luminosity plane consistent with other known Milky Way dwarf galaxies, which supports the findings from our previous spectroscopic follow-up. Cen I has a well-defined morphology that lacks any clear evidence of tidal disruption, whereas Eri IV hosts a significant extended feature with multiple possible interpretations.

Unified Astronomy Thesaurus concepts: Dwarf galaxies (416); Galaxy structure (622); Stellar populations (1622); Direct imaging (387)

Materials only available in the online version of record: machine-readable tables

1. Introduction

Ultrafaint dwarfs (UFDs) are the oldest ($\tau \gtrsim 13.0$ Gyr), faintest ($L \lesssim 10^5 L_\odot$, $M_V \gtrsim -7.7$), least massive ($M \lesssim 10^5 M_\odot$), most metal-poor, and most dark-matter-dominated galactic systems known in the Universe (J. D. Simon 2019). Therefore, they can be used as a unique laboratory to test the nature of dark matter, the validity of Lambda cold dark matter (Λ CDM), and galaxy formation on the smallest scales (e.g., D. H. Weinberg et al. 2015; J. S. Bullock & M. Boylan-Kolchin 2017;

A. X. González-Morales et al. 2017; L. E. Strigari 2018; M. Safarzadeh & D. N. Spergel 2020).

Over the past decade, there has been significant progress in the discovery space of UFDs around the Milky Way (MW; see J. D. Simon 2019, and references therein). However, most newly discovered systems reside at the very limit of the survey data in which they were discovered, and their true nature remains uncertain, partially due to the lack of deep and wide-field imaging. New ultrafaint satellites only have a handful of detectable stars in the discovery data with which to infer their properties. Therefore, it is imperative to follow up new systems to derive robust measurements of their structural parameters, distances, and luminosities, as well as to understand whether a system is clearly disrupting. These findings should then be interpreted in the context of known UFD galaxies.

In this paper we focus on Centaurus I (Cen I) and Eridanus IV (Eri IV), which were discovered in the DECam Local

* This paper includes data gathered with the 6.5 m Magellan Telescopes at Las Campanas Observatory, Chile.



Original content from this work may be used under the terms of the [Creative Commons Attribution 4.0 licence](https://creativecommons.org/licenses/by/4.0/). Any further distribution of this work must maintain attribution to the author(s) and the title of the work, journal citation and DOI.

Table 1
Summary of Magellan/Megacam Observations and Field Completeness

Dwarf Name	UT Date	Filter	Exp (s)	50% (mag)	90% (mag)
Cen I	2022 Jan 28	<i>g</i>	7 × 300	27.43	25.89
	2022 Jan 28	<i>r</i>	7 × 300	26.92	25.16
Eri IV	2022 Feb 2	<i>g</i>	6 × 300	25.37	24.11
	2022 Feb 2	<i>r</i>	6 × 300	25.02	23.45

Volume Exploration survey (DELVE;¹⁷ Cen I, S. Mau et al. 2020; Eri IV, W. Cerny et al. 2021). Both systems were identified using the simple¹⁸ algorithm. This algorithm searches for local spatial overdensities consistent with old and metal-poor stellar populations and has been used to discover over 30 MW satellites (e.g., K. Bechtol et al. 2015; A. Drlica-Wagner et al. 2015; S. Mau et al. 2019, 2020; W. Cerny et al. 2021, 2023c, 2023b, 2023a, 2025; M. McNanna et al. 2024; C. Y. Tan et al. 2025). C. E. Martínez-Vázquez et al. (2021) detected three RR Lyrae stars in Cen I and used them to determine a distance of $D = 117.7 \pm 0.1$ kpc (± 4 kpc systematic error). M. E. Heiger et al. (2024) observed 34 member stars of Cen I and 28 member stars of Eri IV using the Inamori Magellan Areal Camera and Spectrograph (IMACS)/Magellan. They measured the velocity and metallicity dispersions ($\sigma_v = 4.2^{+0.6}_{-0.5}$ km s⁻¹, $\sigma_{[\text{Fe}/\text{H}]} = 0.38^{+0.07}_{-0.05}$ for Cen I; $\sigma_v = 6.1^{+1.2}_{-0.9}$ km s⁻¹, $\sigma_{[\text{Fe}/\text{H}]} = 0.20 \pm 0.09$ for Eri IV) and concluded that the systems are dark matter dominated and exhibit properties largely consistent with other known UFDs.

Interestingly, both systems show tentative signs of tidal disruption, manifested by nearby stellar overdensities in the discovery data. It is essential to investigate these features with deeper follow-up observations, as including unbound stars in dynamical analyses could result in overestimated dark matter masses, and theoretical models attempting to replicate dwarf properties would be based on incorrect luminosities. Here we examine their outer structures, search for extremely low surface brightness extensions, and assess whether these systems are in dynamical equilibrium.

The paper is organized as follows: In Section 2, we describe the observations and the data reduction. Section 3 discusses our analysis of the data regarding the systems’ distances, their structural properties, their absolute magnitudes, and the presence of any extended structures, and we search for potential new member stars in Gaia. We discuss the results of our analysis and their importance in Section 4. Finally, we summarize our main results in Section 5.

2. Observations and Data Reduction

Cen I and Eri IV were observed in the *g* and *r* bands using Megacam at the *f*/5 focus on the Magellan Clay telescope. The data for Cen I and Eri IV were taken on 2022 January 28 and 2022 February 2, respectively. Magellan/Megacam uses 36 2048 × 4608 pixel CCDs, each with a scale of 0.08 pixel⁻¹ (which were binned 2 × 2). This yields a field of view (FOV) of 24′ × 24′ (B. McLeod et al. 2015). We obtained 7 × 300 s exposures in *g* and *r* for Cen I and 6 × 300 s in *g* and *r* for Eri IV (see Table 1). The data were reduced using the Megacam

pipeline developed at the Harvard-Smithsonian Center for Astrophysics by M. Conroy, J. Roll, and B. McLeod; this process includes detrending the data and performing astrometry. We then stack the individual dithered frames with SWarp (E. Bertin et al. 2002).

We perform point-spread function photometry using the DAOPHOTII/ALLSTAR software (P. B. Stetson 1994), and we follow the methodology detailed in B. Mutlu-Pakdil et al. (2018). We run ALLSTAR twice: first on the final stacked image, and then again on the final stacked image after subtracting the stars found in the first run. This methodology allows us to recover much fainter sources. We cull our catalog by removing objects that are not point sources, i.e., we remove outliers in χ^2 versus magnitude, magnitude error versus magnitude, and sharpness versus magnitude. We positionally match our source catalogs derived from the *g*- and *r*-band images using a maximum matching radius of 0.5. Only those point sources detected in both bands are used to create our final catalog for both systems.

We calibrate the output of our stellar photometry by matching with DELVE data release 2 (DR2; A. Drlica-Wagner et al. 2022). We use all stars within the FOV where $17.5 < g < 21$ and $17.5 < r < 21$ for calibration. We correct for Galactic extinction on a star-by-star basis using the D. J. Schlegel et al. (1998) dust maps; the average $E(B - V)$ values are 0.127 for Cen I and 0.109 for Eri IV. All quoted magnitudes throughout this paper are the extinction-corrected values. Tables 2 and 3 show the photometric catalogs containing the calibrated magnitudes (uncorrected for extinction), DAOPHOT uncertainties, and Galactic extinction for Cen I and Eri IV, respectively.

We use the DAOPHOT ADDSTAR routine to inject artificial stars into the data; this allows us to determine our photometric uncertainties and completeness as a function of magnitude and color. Following B. Mutlu-Pakdil et al. (2018), we inject artificial stars into our images on a grid. The *r*-band magnitudes range from 18 to 29 mag, where the values take on fainter magnitudes with an exponentially increasing probability. The *g*-band magnitudes are randomly selected based on the $g - r$ color ranging from -0.5 to 1.5 mag. We perform the artificial star injections 10 different times; each iteration inserts $\sim 100,000$ artificial stars in each field. We then run DAOPHOT and ALLSTAR twice on the images containing the artificial stars in the exact same manner used on the real data. We require the same point-source selection criteria on χ^2 , magnitude error, and sharpness as was required on the real data. We use these artificial star catalogs to determine our 50% and 90% completeness (see Table 1) and photometric uncertainties.

3. Analysis

3.1. Color–Magnitude Diagrams

The left panels of Figures 1(a) and (b) show the color–magnitude diagrams (CMDs) for Cen I and Eri IV that include stars within one half-light radius (as determined in Section 3.3; see Table 4). Plotted in red are 13.0 Gyr, $[\text{Fe}/\text{H}] = -2.2$ PARSEC isochrones (A. Bressan et al. 2012). This corresponds to the best-fit isochrone as determined in Section 3.2. The magenta error bars show the mean photometric errors in color and magnitude as determined by the artificial star tests (see Section 2). These errors are plotted at an arbitrary color for

¹⁷ <https://delve-survey.github.io/>

¹⁸ <https://github.com/DarkEnergySurvey/simple>

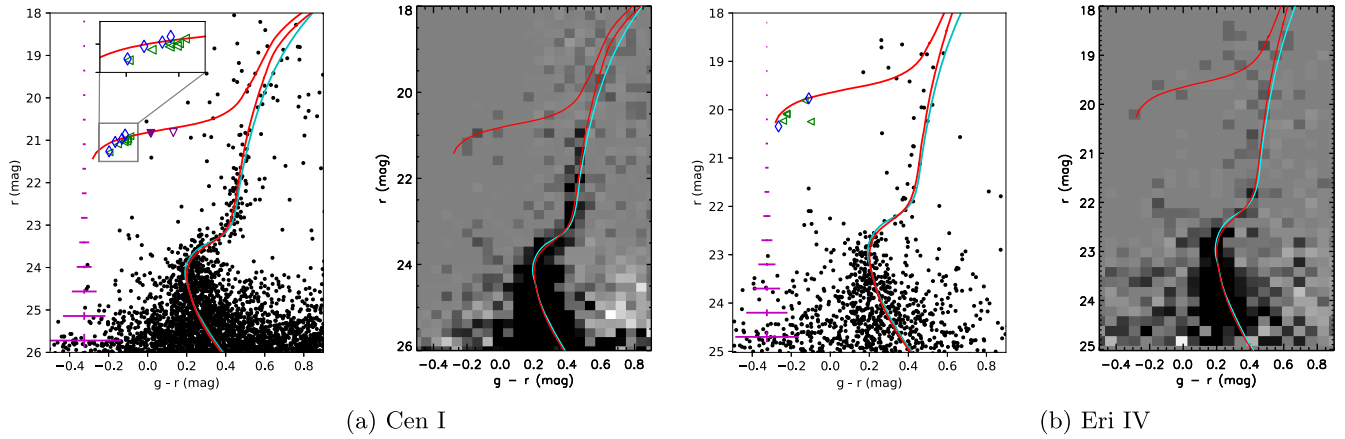


Figure 1. CMD and Hess diagrams for (a) Cen I and (b) Eri IV. We only include stars within the half-light radius for a given UFD (Section 3.3). Candidate HB stars within the half-light radius are shown as blue diamonds, candidate HB stars within the FOV are shown as green triangles, and RR Lyrae stars from C. E. Martínez-Vázquez et al. (2021) are shown as purple triangles for Cen I only (the filled triangle is within the half-light radius; the other is within the FOV). Magenta error bars show the mean color and magnitude errors in the CMDs. The red lines are PARSEC isochrones with a 13.0 Gyr stellar population and metallicity $[\text{Fe}/\text{H}] = -2.2$. The cyan lines are 13.0 Gyr DSEP isochrones with metallicity $[\text{Fe}/\text{H}] = -2.4$ and alpha enhancement $[\alpha/\text{Fe}] = 0.4$ shown for comparison purposes. The isochrones are shifted to the distance modulus derived in Section 3.2: $m - M = 20.39$ for Cen I and $m - M = 19.22$ for Eri IV.

Table 2
Cen I Photometry in the DELVE Photometric System

Star No.	α (deg J2000.0)	δ (deg J2000.0)	g (mag)	δg (mag)	A_g (mag)	r (mag)	δr (mag)	A_r (mag)
0	189.40289	-41.054473	19.360	0.003	0.334	18.449	0.003	0.225
1	189.37668	-40.915770	19.528	0.007	0.357	18.709	0.004	0.240
2	189.47749	-41.040136	19.637	0.010	0.349	18.791	0.010	0.234
3	189.40136	-41.048903	19.611	0.004	0.335	18.828	0.003	0.225
4	189.37714	-40.890137	19.998	0.003	0.359	19.251	0.016	0.241

(This table is available in its entirety in machine-readable form in the [online article](#).)

Table 3
Eri IV Photometry in the DELVE Photometric System

Star No.	α (deg J2000.0)	δ (deg J2000.0)	g (mag)	δg (mag)	A_g (mag)	r (mag)	δr (mag)	A_r (mag)
0	76.422511	-9.366627	18.784	0.001	0.326	18.055	0.003	0.234
1	76.558057	-9.494939	18.961	0.002	0.326	18.272	0.003	0.233
2	76.535325	-9.493604	19.138	0.004	0.332	18.461	0.003	0.237
3	76.295080	-9.380901	19.561	0.002	0.339	18.911	0.004	0.243
4	76.341677	-9.361639	19.668	0.003	0.325	19.014	0.002	0.233

(This table is available in its entirety in machine-readable form in the [online article](#).)

convenience. Open blue diamonds are potential horizontal branch (HB) stars within the half-light radius, and green triangles are potential HB stars within the FOV: a total of 11 in Cen I and 7 in Eri IV. Newly discovered HB candidates are presented in Tables 5 and 6. In the CMD for Cen I we show two RR Lyrae stars from C. E. Martínez-Vázquez et al. (2021) as purple triangles; the third star from that study lies outside our FOV. The filled triangle lies within our half-light radius, while the other RR Lyrae star is within the FOV.

The right panels of Figures 1(a) and (b) show background-subtracted binned Hess diagrams. Hess diagrams highlight the number density of stars in regions of the CMD. The background is derived from a region beyond a $12'$ radius; this radius is well outside the main body of Cen I and Eri IV. The isochrones of the Hess diagrams are the same as the PARSEC isochrones on the CMDs.

3.2. Distance

We use a CMD-fitting technique to determine the distance modulus, similar to the method described in B. Mutlu-Pakdil et al. (2018). This methodology considers main-sequence (MS), red giant branch (RGB), and HB stars; we compare the UFD CMDs with empirical globular cluster (GC) fiducials and theoretical isochrones. MS and RGB stars are handled separately from HB stars when deriving the distance modulus. For the MS and RGB stars of Cen I we consider two metal-poor PARSEC isochrones: $[\text{Fe}/\text{H}] = -2.2$ and -2.0 ($[\text{Fe}/\text{H}] = -2.2$ is the lowest-metallicity PARSEC isochrone available). We apply the same PARSEC isochrones to the Eri IV data. The stellar ages (13.0 Gyr) of the isochrones were chosen to be consistent with the discovery papers. We shift the distance modulus ($m - M$) applied to the isochrone in

Table 4
Structural Properties of Cen I and Eri IV

Parameter	Cen I	Eri IV
α_{2000} (deg)	$189^{\circ}5908 \pm 9.5$	$76^{\circ}4246 \pm 16.4$
δ_{2000} (deg)	$-40^{\circ}9043 \pm 10.5$	$-9^{\circ}5189 \pm 15.3$
$m - M$ (mag)	20.39 ± 0.08	19.22 ± 0.11
D (kpc)	119.8 ± 4.1	69.9 ± 3.6
M_V (mag)	-5.39 ± 0.19	-3.55 ± 0.24
r_h (arcmin)	2.60 ± 0.30	3.24 ± 0.48
r_h (pc)	90.6 ± 11	65.9 ± 10
$r_{1/2}$ (arcmin)	2.08 ± 0.25	2.78 ± 0.45
$r_{1/2}$ (pc)	72.6 ± 9.2	56.5 ± 9.5
ϵ	0.36 ± 0.05	0.26 ± 0.09
P.A. (deg)	10 ± 4	75 ± 26
v_{sys} (km s $^{-1}$)	44.9 ± 0.8	$-31.5^{+1.3}_{-1.2}$
σ_v (km s $^{-1}$)	$4.2^{+0.6}_{-0.5}$	$6.1^{+1.2}_{-0.9}$
[Fe/H] (dex)	-2.57 ± 0.08	$-2.87^{+0.08}_{-0.07}$
$\sigma_{[\text{Fe}/\text{H}]}$ (dex)	$0.38^{+0.07}_{-0.05}$	0.20 ± 0.09
$\mu_{\alpha} \cos \delta$ (mas yr $^{-1}$)	-0.14 ± 0.05	0.22 ± 0.06
μ_{δ} (mas yr $^{-1}$)	-0.19 ± 0.04	-0.11 ± 0.05
r_{peri} (kpc)	32^{+12}_{-8}	43 ± 11

Note. α_{2000} : the R.A. (J2000.0). δ_{2000} : the decl. (J2000.0). $m - M$: the distance modulus. D : the distance of the galaxy in kpc. M_V : the absolute V -band magnitude. r_h : the elliptical half-light radius along the semimajor axis. $r_{1/2}$: the geometric mean of the half-light radius. ϵ : ellipticity, which is defined as $\epsilon = 1 - b/a$, where b is the semiminor axis and a is the semimajor axis. P.A.: position angle. v_{sys} : systemic radial velocity in the heliocentric frame. σ_v : velocity dispersion. [Fe/H]: mean metallicity. $\sigma_{[\text{Fe}/\text{H}]}$: metallicity dispersion. $\mu_{\alpha} \cos \delta$: systemic proper motion in R.A. μ_{δ} : systemic proper motion in decl. r_{peri} : orbital pericenter. Values α_{2000} through the position angle (P.A.) are calculated in this work; values v_{sys} through r_{peri} are from M. E. Heiger et al. (2024).

0.025 mag intervals over 2 mag. With each shift, we count the number of stars that are consistent with the isochrone when taking into account the photometric uncertainties of the data. When the photometric errors are <0.1 mag, we inflate the uncertainty to 0.1 mag.

For Cen I, we select all stars with $r \leq 24$ mag that are within one half-light radius ($r_h = 2/60$) of its center. We shift the distance modulus from 19.5 to 21.5 mag; this is consistent with the distance modulus reported by the discovery paper. We also run this procedure over background stars selected from an equal-area background region offset $\gtrsim 11'$ from the center of Cen I. The best-fit distance modulus is when the isochrone fit yields the maximum number of stars after accounting for background contamination: $m - M = 20.45$ for [Fe/H] = -2.2 (118 stars) and $m - M = 20.30$ for [Fe/H] = -2.0 (122 stars). Likewise, for Eri IV we select stars with $r \leq 23$ mag and within one half-light radius ($r_h = 3/24$) of its center. The distance modulus is shifted from 18.5 to 20.5 mag, and we account for background stars similarly to Cen I. The maximizing distance moduli for Eri IV are $m - M = 19.23$ for [Fe/H] = -2.2 (37 stars) and $m - M = 19.21$ for [Fe/H] = -2.0 (38 stars). We determine the uncertainties on each fit using a 100-iteration bootstrap resampling analysis.

We also derive a distance modulus for both dwarfs using their potential HB stars within the FOV. This is 11 stars for Cen I and 7 stars for Eri IV (see Figure 1). The number of potential HB stars in Cen I and Eri IV is comparable to that for other well-studied systems (e.g., D. J. Sand et al. 2010;

S. E. Koposov et al. 2015; R. R. Muñoz et al. 2018; D. Homma et al. 2019). We fit the M92 GC HB fiducial (E. J. Bernard et al. 2014) to our HB star candidates by minimizing the sum of squares of the difference between the data and the fiducial. We measure the r magnitude offset a given HB star lies from the fiducial, shift the distance modulus of the fiducial by 0.025 mag, and remeasure the offset. This process is repeated through 2 mag. The shift that minimizes the sum of squares is adopted as the distance modulus. We opt to use empirical HB fiducial tracks rather than HB isochrones, as HB isochrones are historically more difficult to model and have a certain level of uncertainty associated with them (e.g., A. Pietrinferni et al. 2004). We use M92 ($m - M = 14.65$ mag; E. J. Bernard et al. 2014) specifically because it is one of the most ancient, metal-poor, and well-studied GCs.

Using this HB distance modulus measurement technique, we find $m - M = 20.43$ for Cen I and $m - M = 19.18$ for Eri IV. To determine the uncertainty associated with the HB distance modulus, we implement jackknife resampling (i.e., we remove a single HB star from the sample and remeasure the distance modulus). This technique accounts for the possibility of interloper stars contaminating our HB sample. The standard deviation of the jackknife-resampled distance moduli is adopted as the uncertainty for this measurement. Jackknife resampling does not change the distance modulus measurement for Cen I. The distance modulus for Eri IV is in the range of $19.15 \leq m - M \leq 19.18$ with a standard deviation of ~ 0.01 after resampling.

To find the total distance modulus errors, we add (in quadrature) the uncertainty derived from the bootstrap analysis applied to MS/RBG stars and the uncertainty from the jackknife-resampled HB stars. The distance modulus we adopt for Cen I and Eri IV is the mean value between the two methods (MS/RGB star counting and HB fiducial fitting); these results are shown in Table 4.

Old, low-metallicity isochrones exhibit minimal variation based on the chosen age and metallicity. Separate libraries, such as the Dartmouth Stellar Evolution Database (DSEP; A. Dotter et al. 2008), closely resemble PARSEC isochrones in this regime. Using DSEP isochrones ([Fe/H] = -2.4 , -2.2 and $[\alpha/\text{Fe}] = 0.4$), we derive distances consistent with the PARSEC models within the uncertainties quoted in Table 4; we show one DSEP isochrone in Figure 1 for reference. Ultimately, we choose the PARSEC models to remain consistent with the discovery papers.

3.3. Structural Properties

To determine the structural properties of Cen I and Eri IV, we use a maximum likelihood analysis described in D. J. Sand et al. (2009; see also N. F. Martin et al. 2008). In short, the routine fits an exponential profile to the 2D distribution of stars associated with each UFD. We select stars consistent within our 90% completeness measurement and an [Fe/H] = -2.2 PARSEC isochrone in color-magnitude space after accounting for photometric uncertainties. This is 812 stars for Cen I and 243 stars for Eri IV. The structural parameters from the discovery papers (S. Mau et al. 2020; W. Cerny et al. 2021) are adopted as the input parameters for the initial analysis. The data are bootstrap resampled 1000 times; the structural parameters are recalculated for each such resampling, which determines the uncertainty on the measurement. The resulting structural parameters are shown in Table 4.

Table 5
Newly Identified Potential Member Stars in Cen I

Gaia ID	R.A. (deg)	Decl. (deg)	g (mag)	r (mag)	$\mu_{\alpha} \cos \delta$ (mas yr ⁻¹)	μ_{δ} (mas yr ⁻¹)	Type	Method
6146244710500639104	189.454650	-40.949242	20.64	20.10	-1.474 ± 0.632	0.972 ± 0.589	RBG	2
...	189.536440	-40.870731	20.88	21.00	HB ^a	...
...	189.547430	-40.910299	20.93	21.03	HB ^a	...
...	189.550540	-40.957694	20.89	20.99	HB ^a	...
6146244366903299328	189.551620	-40.922743	18.86	18.10	-2.851 ± 0.165	-1.761 ± 0.144	RGB	2
...	189.567240	-40.883106	20.75	20.87	HB ^a	...
...	189.587720	-40.935858	21.06	21.26	HB ^a	...
...	189.596760	-40.900816	20.87	21.04	HB ^a	...
...	189.603500	-40.918177	20.83	20.96	HB ^a	...
6146234097636409344	189.604605	-40.911450	20.38	19.72	0.171 ± 0.489	-0.479 ± 0.414	RGB	1
...	189.617670	-40.960118	20.95	21.10	HB ^a	...
...	189.626020	-40.850364	20.93	21.05	HB ^a	...
...	189.632750	-40.839181	21.09	21.28	HB ^a	...
6146233754039010048	189.635114	-40.951360	19.55	18.89	-0.160 ± 0.321	-0.469 ± 0.250	RBG	1, 2
...	189.643710	-40.905551	20.81	20.90	HB ^a	...
6146233406146774784	189.731830	-40.905546	19.33	18.66	-1.095 ± 0.234	-0.890 ± 0.224	RGB	2
6146257457963749248	189.805530	-40.828194	20.57	20.02	-0.916 ± 0.703	-1.049 ± 0.651	RGB	2

Notes. Method 1 uses the conservative selection, and method 2 uses the flexible selection, as described in Section 3.6. Entries with no Gaia ID are potential HB stars used in the distance determination (Section 3.2) but that do not have Gaia observations.

^a Denotes star used in distance determination.

Table 6
Newly Identified Potential Member Stars in Eri IV

Gaia ID	R.A. (deg)	Decl. (deg)	g (mag)	r (mag)	$\mu_{\alpha} \cos \delta$ (mas yr ⁻¹)	μ_{δ} (mas yr ⁻¹)	Type	Method
3182741431156735488	76.295080	-9.380901	19.22	18.67	1.305 ± 0.246	0.300 ± 0.206	RGB	2
3182741671674916608	76.341677	-9.361639	19.34	18.78	1.749 ± 0.213	0.497 ± 0.196	RGB	2
3182738063902340736	76.352797	-9.422692	19.59	19.05	0.065 ± 0.280	0.053 ± 0.240	RGB	2
3182721639948162176	76.372800	-9.600543	19.68	19.81	0.768 ± 0.468	-0.609 ± 0.381	HB ^b	2
3182722911258501888	76.400357	-9.559472	19.94	19.70	0.066 ± 0.399	0.037 ± 0.353	HB/RRL	1
3182718135254812672	76.412174	-9.676816	19.47	18.92	0.749 ± 0.271	-0.038 ± 0.238	RGB	2
3182724629244570496	76.423206	-9.519234	19.35	18.94	0.121 ± 0.257	-0.031 ± 0.236	RGB	1
3182724457445870848	76.432246	-9.533512	19.87 ^a	20.07 ^a	0.859 ± 0.525	-0.564 ± 0.500	HB	1
3182723843267791616	76.461253	-9.532902	19.32	18.85	0.282 ± 0.237	-0.036 ± 0.212	RGB	1, 2
3182724972841956608	76.462523	-9.514698	20.60	20.17	0.302 ± 0.764	0.062 ± 0.704	RGB	1
3182725114578785792	76.484535	-9.490527	19.87	20.10	0.908 ± 0.526	-0.219 ± 0.506	HB ^b	1, 2
3182747581549809024	76.538458	-9.505236	19.85	20.08	0.278 ± 0.549	0.345 ± 0.503	HB ^b	2
3182670443938116864	76.565750	-9.682317	20.87	20.41	0.850 ± 0.791	0.655 ± 0.850	RGB	2
3182744523533084416	76.584477	-9.519372	20.15	20.25	-0.303 ± 0.544	-0.279 ± 0.445	HB ^b	2

Notes. Method 1 uses the conservative selection, and method 2 uses the flexible selection, as described in Section 3.6.

^a This star falls in a chip gap and has unreliable photometry, so we report the DELVE DR3 photometry.

^b Denotes star used in distance determination.

3.4. Absolute Magnitude

We derive the absolute magnitudes for Cen I and Eri IV by using the same procedure as in B. Mutlu-Pakdil et al. (2018), as was first described in N. F. Martin et al. (2008). We construct a densely populated ($N \sim 45,000$) artificial CMD where stars are consistent with our completeness and photometric uncertainties. The luminosity functions are generated using the PARSEC database with $[\text{Fe}/\text{H}] = -2.2$, and we assume a Salpeter initial mass function (E. E. Salpeter 1955). We randomly select N number of stars from our artificial CMD (over the same magnitude range as was used to derive the structural properties), where N was derived from the exponential profile fits (Section 3.3). We calculate the total luminosity by adding the

fluxes of these randomly selected stars and estimating the flux of the faint, unresolved component of the galaxy using the adopted luminosity function. We perform 1000 realizations in this way, and we take the mean as our absolute magnitude and its standard deviation as our uncertainty. We account for variation in the distance modulus and number of stars by allowing either value to vary by their associated errors; this process is repeated 100 separate times. The errors are added in quadrature to produce the total uncertainty on our absolute magnitude measurement. We account for HB stars by adding the fluxes of the HB candidates within our FOV. This yields an absolute magnitude of $M_V = -5.39 \pm 0.19$ mag for Cen I and $M_V = -3.55 \pm 0.24$ mag for Eri IV (see Table 4). For each

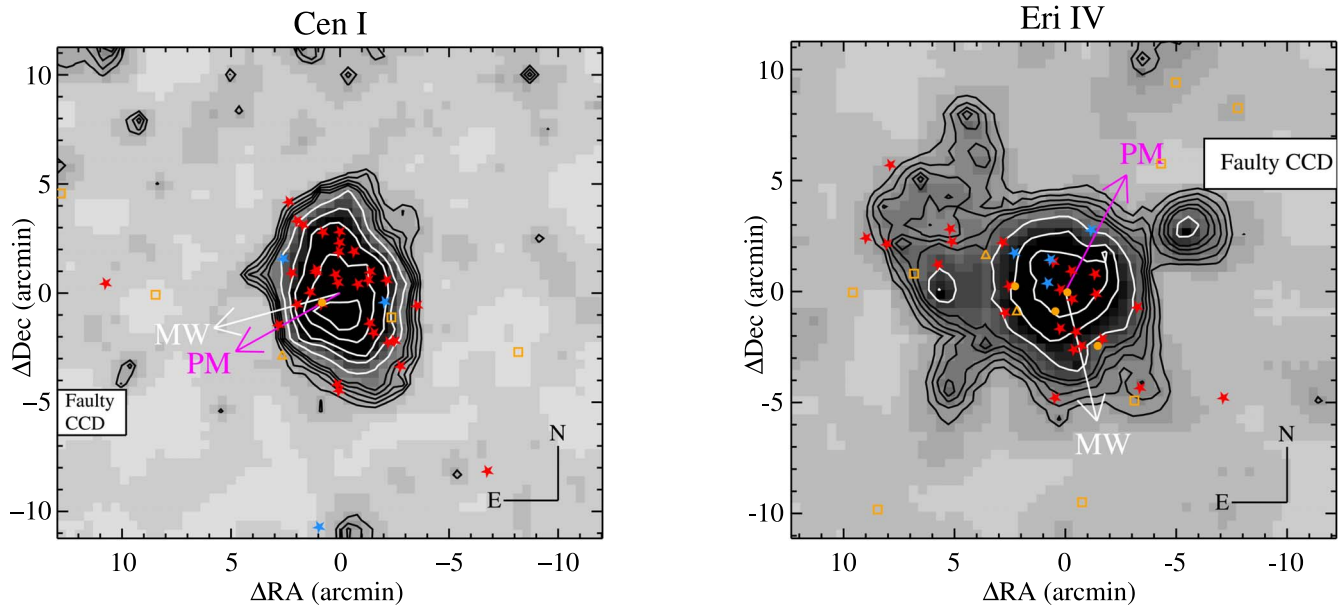


Figure 2. The smoothed matched-filter maps for Cen I (left) and Eri IV (right), where the image center corresponds to the R.A. and decl. reported in Table 4; north is up, and east is to the left. Overplotted are the contour levels above the rms of the background for each UFD, which are $3\sigma, 4\sigma, 5\sigma, 6\sigma, 7\sigma, 10\sigma, 15\sigma, 20\sigma, 30\sigma, 40\sigma$ for Cen I and $3\sigma, 4\sigma, 5\sigma, 6\sigma, 7\sigma, 10\sigma, 15\sigma, 20\sigma$ for Eri IV. The white arrow denotes the direction to the Galactic center, and the magenta arrow marks the solar-reflex-corrected proper motion. The blue and red stars represent the location of member stars observed by M. E. Heiger et al. (2024), where blue are HB stars and red are RGB stars. New potential members (see Section 3.6) are shown in orange: circles are those found using the conservative method, squares are those found using the flexible method, and triangles are those recovered with both methods. Note that faulty CCDs are shown in the lower left corner for Cen I and in the upper right corner for Eri IV.

system, the impact of HB candidates on the absolute magnitude falls within the stated uncertainty.

3.5. Extended Structure Search

We investigate whether our targets have undergone tidal disruption, which might manifest in the form of extended structures and/or stellar streams. This analysis holds particular significance because the discovery data suggested the presence of extended structures; however, subsequent spectroscopic observations (M. E. Heiger et al. 2024) disfavor tidal disruption in Cen I or Eri IV. We use a matched-filter algorithm, which maximizes the signal-to-noise ratio of data against the background. The concept of applying matched-filter algorithms to study tidal disruptions was introduced by C. M. Rockosi et al. (2002) and initially applied to GCs. This approach has since been adopted to investigate newly identified UFDs for signs of extended structures (e.g., D. J. Sand et al. 2012; B. Mutlu-Pakdil et al. 2018).

To apply the matched-filter technique to our data, we use the same simulated stars as used in Section 3.4 as the signal CMD (i.e., stars simulated to match an old, metal-poor PARSEC isochrone, accounting for photometric errors and magnitudes brighter than the 90% completeness threshold). Simulated data are preferable to the observed data, which can be sparsely populated and contaminated with background/foreground objects (D. J. Sand et al. 2012). For the background CMD, we use the real stars well outside the half-light radius of both UFDs. The matched-filter stellar density maps are shown in Figure 2; both maps have been spatially binned to a pixel size of $25''$ and smoothed with a Gaussian width 1.0 times the pixel size. The background and variance of the smoothed maps are determined with IDL’s MMM routine. The main body of each satellite is clearly visible in each map. The white arrows in Figure 2 represent the direction to the Galactic center, and the

magenta arrows denote the solar-reflex-corrected proper motions from M. E. Heiger et al. (2024). The spectroscopic member stars observed by M. E. Heiger et al. (2024) are shown in red (RGB) and blue (HB), and the potential member stars discussed in Section 3.6 are shown in orange.

Both Cen I and Eri IV present as clear overdensities against the background. Cen I exhibits a well-defined morphology lacking any clear extended features. For Eri IV, there appears to be a significant feature positioned to the northeast of the main body. This feature shows up as a $3\sigma, 4\sigma, 5\sigma, 6\sigma$, and 7σ overdense region depending on the location. We use the statistical tests outlined in S. M. Walsh et al. (2008) and D. J. Sand et al. (2010) to assess whether this feature results from small number statistics or background features. We bootstrap resample Eri IV’s entire photometric catalog, and we resample the stars that are consistent with the isochrone and uncertainties. For each such resampling we update the smoothed maps and inspect regions of particular interest. These tests recover the extended feature for all of the resamplings. The “nugget” situated below the faulty CCD varies in significance during the resamplings and goes away in one-third of the tests. Additionally, we visually inspect these regions in the images and find no artifacts or galaxy clusters that may masquerade as a stellar overdensity. We keep this in mind when considering the overall morphology of Eri IV, and we discuss its implications in more depth in Section 4.

3.6. Potential Member Stars in Gaia

We use our deep photometry and the precise astrometry of Gaia Early Data Release 3 (EDR3; Gaia Collaboration et al. 2016, 2021) to search for potential new member stars using two separate methods. The first method cross-matches Gaia objects with our photometry after applying a CMD filter described in A. B. Pace & T. S. Li (2019) and A. B. Pace et al. (2022). A

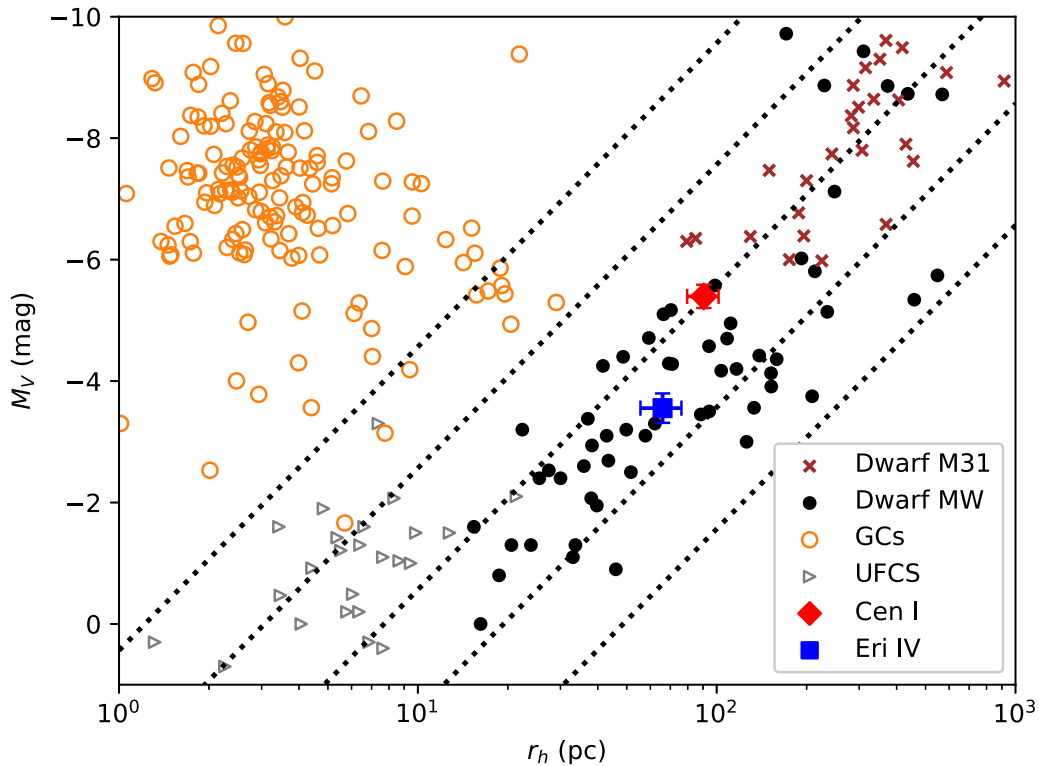


Figure 3. Half-light radius along the semimajor axis (r_h) against the absolute magnitude (M_V) for a number of dwarf galaxies/GCs. Cen I and Eri IV are shown by the red diamond and blue square, respectively. Brown crosses are M31 dwarf galaxies (e.g., E. J. Tollerud et al. 2012; N. F. Martin et al. 2016; K. L. Rhode et al. 2023), black circles are MW dwarf galaxies, orange open circles are GCs from W. E. Harris (2010), and gray triangles are ultrafaint compact satellites (UFCS). The dotted black lines denote a constant surface brightness. Data in this figure were taken from the Local Volume Database (A. B. Pace 2024).

Gaussian mixture model composed of an MW background and a satellite component is applied to the proper motions and spatial positions of these stars. Similar to A. B. Pace et al. (2022), we assume Gaussian priors for the structural parameters derived in Section 3.3. This conservative method weights the probability of a star’s membership based on its distance from the center of the UFD. We find two probable member stars in Cen I and six in Eri IV.

We also explore the entire FOV by cross-matching stars that agree with our CMD selection used in Section 3.3 with Gaia EDR3. We keep stars that satisfy the following criteria: $\text{ruwe} < 1.4$, $\text{astrometric_excess_noise} < 2$, and stars that are consistent with zero parallax ($\varpi - 3\sigma_\varpi > 0$). Furthermore, we exclude stars that are inconsistent with the proper motions of the stars presented in M. E. Heiger et al. (2024). This flexible selection method yields four additional stars in Cen I and eight additional stars in Eri IV. The potential new member stars in Cen I and Eri IV are listed in Tables 5 and 6, respectively. They are ideal targets for a future spectroscopic study. Their spatial positions are shown in Figure 2 in orange. Two of Eri IV’s newly identified potential member stars are situated near the extended feature.

4. Discussion

Figure 3 shows Cen I (red diamond) and Eri IV (blue square) in the size–luminosity plane, relative to Local Group dwarf galaxies and GCs. Black circles are the most up-to-date confirmed/candidate MW dwarf satellites (see A. W. McConnachie 2012; A. Drlica-Wagner et al. 2015, 2016; D. Kim & H. Jerjen 2015; S. E. Koposov et al. 2015, 2018; N. F. Martin et al. 2015; D. Crnojević et al. 2016; G. Torrealba et al. 2016a, 2016b, 2018;

J. L. Carlin et al. 2017; Y. Choi et al. 2018; D. Homma et al. 2018, 2019, 2024; R. R. Muñoz et al. 2018; B. Mutlu-Pakdil et al. 2018; M. Y. Wang et al. 2019; S. Mau et al. 2020; A. G. Moskowicz & M. G. Walker 2020; J. D. Simon et al. 2020; S. A. Cantu et al. 2021; W. Cerny et al. 2021, 2023c, 2023b; A. P. Ji et al. 2021; H. Richstein et al. 2022; S. E. T. Smith et al. 2023). The data in Figure 3 were taken from the Local Volume Database (A. B. Pace 2024). Both Cen I and Eri IV are consistent with the population of known dwarf galaxies. We discuss each satellite’s derived properties in detail in the following subsections.

4.1. Cen I

The deep imaging of Cen I shows a well-populated MS, an easily identifiable RGB, 11 potential HB candidates within the FOV (four within one r_h), and a handful of blue stragglers (Figure 1, left panel). The stellar population is consistent with an age of $\tau \approx 13.0$ Gyr and a metallicity of $[\text{Fe}/\text{H}] \sim -2.2$. We find the distance to Cen I to be $D = 119.8 \pm 4.1$ kpc ($m - M = 20.39 \pm 0.08$ mag); this is in good agreement with the results reported in S. Mau et al. (2020) ($D = 116.3^{+1.6}_{-0.6}$ kpc, $m - M = 20.33^{+0.03}_{-0.01} \pm 0.1$ mag). Our measurement also agrees well with C. E. Martínez-Vázquez et al. (2021), who derived the distance using three RR Lyrae stars. They found $D = 117.7 \pm 0.1$ kpc, $m - M = 20.354 \pm 0.002$ mag with systematic errors of 4 kpc and 0.07 mag. We show two of the RR Lyrae stars in Figure 1; the third star was outside our FOV. Three RR Lyrae stars is consistent with the expected number (1–12 stars) for UFDs of similar magnitudes (C. E. Martínez-Vázquez et al. 2019, 2021).

We robustly constrain the structural parameters (i.e., R.A., decl., r_h , ϵ , P.A.) of Cen I using a maximum likelihood analysis (see Section 3.3); these results are shown in Table 4. Our structural parameters agree very well with the values reported in the discovery data, with decreased uncertainties on most of the measurements. Cen I occupies a space on the size–luminosity plane consistent with other confirmed UFDs (Figure 3). Our work further supports the UFD nature of Cen I and strengthens the findings of S. Mau et al. (2020) and M. E. Heiger et al. (2024).

Dynamical interactions between satellites and their host galaxies, such as tidal stripping, serve as feedback mechanisms that reduce the central mass of satellites. Mass-to-light (M/L) ratios are calculated under the assumption of dynamical equilibrium. If a system is tidally disrupting, then dark matter estimates (via velocity dispersion) would be inaccurate. Therefore, it is crucial to understand the dynamical state and morphologies of UFDs. Cen I has a well-defined structure and exists as a clear overdensity in Figure 2. S. Mau et al. (2020) identified a potential tidal feature in the discovery data situated $\sim 10'$ west of Cen I’s center; however, we do not find any evidence for the existence of this feature in our deep, wide-field data. The feature suggested in the discovery paper is potentially due to background contamination in shallow data. M. E. Heiger et al. (2024) did not observe this region spectroscopically, as none of the high-probability member stars reside in this region. The spectroscopic analysis revealed a velocity gradient consistent with zero across Cen I’s semimajor axis (tidally disrupting systems are expected to have a large velocity gradient in the direction of its orbit; e.g., A. P. Ji et al. 2021). Therefore, M. E. Heiger et al. (2024) conclude that Cen I is not tidally disrupting based on the spectroscopic evidence. Due to the lack of any overdensity in the proposed region of disruption, our findings agree with M. E. Heiger et al. (2024), and we conclude that Cen I does not have a tidal feature associated with it.

4.2. Eri IV

The CMD of Eri IV shows an MS with a fair amount of color scatter (due to photometric uncertainties), but there exists a clear MS turnoff. The RGB is less populated compared to Cen I, which aligns with our findings that Cen I is brighter. We find seven potential HB stars within the FOV (two within one r_h) and a number of potential blue stragglers (Figure 1). We find one potential RR Lyrae star (Table 6), which appears in the Gaia DR3 variability catalog (L. Eyer et al. 2023) but is classified as an eclipsing binary. A system with the luminosity of Eri IV is expected to have few, if any, RR Lyrae stars (C. E. Martínez-Vázquez et al. 2019). The stellar population of Eri IV is consistent with an age of $\tau \approx 13.0$ Gyr and a metallicity of $[\text{Fe}/\text{H}] \lesssim -2.2$. We find Eri IV to be marginally closer than initially reported, but consistent within the joint 1σ uncertainty: $D = 69.9 \pm 3.6$ kpc (this work), compared to $D = 76.7^{+4.0}_{-6.1}$ kpc from W. Cerny et al. (2021).

Our structural parameters mostly agree with those reported with the discovery data, i.e., α_{2000} , δ_{2000} , r_h , and the position angle. Our data reveal a less elongated shape for Eri IV: we find $\epsilon = 0.26 \pm 0.09$, and W. Cerny et al. (2021) found $\epsilon = 0.54^{+0.10}_{-0.14}$. We derive an absolute magnitude of $M_V = -3.55 \pm 0.24$ mag, which makes Eri IV fainter than what was previously thought ($M_V = -4.7 \pm 0.2$ mag; W. Cerny et al. 2021). However, had we used the distance modulus from the discovery data

($m - M = 19.42^{+0.01}_{-0.08} \pm 0.1$), we would have calculated $M_V = -3.81 \pm 0.27$ mag, which agrees with our measurement.

Eri IV displays a well-defined central body, a “nugget” situated below the faulty CCD, and an extended feature located to the northeast of the main system (Figure 2, right panel). The nugget varies in significance depending on the smoothing/binning parameters, and it goes away in approximately one-third of our resampling tests. Additionally, none of the spectroscopic member stars or the potential member stars are aligned with this feature. For these reasons, and due to its proximity to the faulty CCD, we cannot confidently claim that this feature is real. The extended feature is situated in the same area as the overdensity described in the discovery paper (W. Cerny et al. 2021, their Figure 1). The authors advised careful interpretation of this feature owing to the limited number of observed stars. M. E. Heiger et al. (2024) spectroscopically observed stars near the main body ($N = 22$) and the extended feature ($N = 6$) of Eri IV. They find a velocity gradient consistent with zero along the semimajor axis. They estimate that the tidal radius at its pericenter is $r_t = 498 \pm 128$ pc, which yields $r_t/r_h \approx 6.6 \pm 0.3$. A system undergoing tidal disruption is thought to have a tidal radius that is approximately equal to its half-light radius (A. B. Pace et al. 2022), and the tidal radius is often approximated as the Jacobi radius (J. Binney & S. Tremaine 2008). These reasons lead M. E. Heiger et al. (2024) to conclude that Eri IV is likely not tidally disrupting. Our updated half-light radius increases the ratio to $r_t/r_h \approx 7.6$. It is worth noting that some cosmological simulations (e.g., FIRE; A. R. Wetzel et al. 2016) find that satellites disrupt well outside the $r_t/r_h \approx 1$ limit, and the Jacobi radius/tidal radius approximation does not always hold (N. Shipp et al. 2023).

Our data suggest that the extension northeast of Eri IV’s center is significant and could *potentially* be the result of tides. This feature persists regardless of the smoothing or binning parameters used to generate the matched-filter map. We also note that the spectroscopically confirmed member stars observed by M. E. Heiger et al. (2024) closely align with this feature, along with two of the potential new members. The extension persists with similar significance when we bootstrap resample Eri IV’s stars (see Section 3.5). This persistence confirms that this region is not the result of background noise or small number statistics. Given that the high significance of this feature is consistently seen across different analysis techniques/parameters and is distinguishable from background noise, it is possible that Eri IV may have experienced tidal interactions leading to the extended structure visible in Figure 2 (right panel).

The spectroscopic evidence does not favor a tidal stripping scenario. The potential tidal debris is misaligned with the predicted orbit of Eri IV, and M. E. Heiger et al. (2024) show that including/excluding the Large Magellanic Cloud does not significantly alter this prediction. Furthermore, M. E. Heiger et al. (2024) show that Eri IV is moving toward its pericenter ($r_{\text{peri}} = 43 \pm 11$ kpc), having been at its apocenter ($r_{\text{apo}} = 135^{+24}_{-13}$ kpc) approximately 1 Gyr ago. It is unlikely that MW tidal forces would play any major role at this location in its orbit; however, see A. H. Riley et al. (2024) and N. Shipp et al. (2024) for simulated streams that form on comparable orbits, including via preprocessing.

Systems undergoing tidal disruption are expected to have moderately large ellipticities, but this is not a requirement (e.g.,

R. R. Muñoz et al. 2008). For example, Tucana III ($\epsilon = 0.2 \pm 0.1$; A. Drlica-Wagner et al. 2015; B. Mutlu-Pakdil et al. 2018; N. Shipp et al. 2018) and Crater II ($\epsilon = 0.12 \pm 0.02$; G. Torrealba et al. 2016a; A. K. Vivas et al. 2020; A. P. Ji et al. 2021) show clear signs of tidal disruption despite relatively small ellipticities. Therefore, Eri IV’s modest ellipticity ($\epsilon = 0.26 \pm 0.09$) does not necessarily conflict with a potential tidal stripping scenario. Ursa Major II (UMa II, D. B. Zucker et al. 2006; R. R. Muñoz et al. 2010, 2018) occupies a similar space to Eri IV on the size–luminosity plane and is thought to be tidally disrupting; however, UMa II does have a high ellipticity ($\epsilon = 0.56$). Eri IV also resembles two MW UFDs in terms of its structural parameters, Pisces II (V. Belokurov et al. 2010; D. J. Sand et al. 2012; H. Richstein et al. 2022) and Coma Berenices (V. Belokurov et al. 2007; R. R. Muñoz et al. 2018), neither of which shows extended features to the same extent as Eri IV. Hercules is a highly elongated UFD long thought to be tidally disrupting, yet conclusive evidence has remained elusive (e.g., B. Mutlu-Pakdil et al. 2020). X. Ou et al. (2024) recently showed that dynamical models of stream formation can replicate Hercules’s morphology, while indicating that any radial velocity gradient via tidal disruption would be undetectable given their sample size of 28 stars.

Our photometric evidence suggests, with high confidence, that the northeast extension is a real feature. One explanation for the feature is that Eri IV is being tidally disrupted, but the sample size of spectroscopic stars is too small to detect a velocity gradient, and/or our orbital assumptions are incorrect. However, tidal disruption is not the only explanation for the extended feature; this region could be interpreted as a stellar halo, captured field stars, or a satellite of Eri IV. A. Chiti et al. (2021) found an extended component (member stars out to $9r_h$) of Tucana II, suggestive of strong bursty feedback or an early merger. Y. Tarumi et al. (2021) show that major mergers of UFDs at early times can produce extended stellar halos similar to Tucana II, and halo production is quite sensitive to the merger mass ratio (e.g., L. Querci et al. 2025). J. Peñarrubia et al. (2024) show that stellar clumps, similar to the extension in Eri IV, can be explained by starless dark matter sub-subhalos capturing field stars. These clumps would contain stellar populations indistinguishable from the host galaxy; M. E. Heiger et al. (2024) found no evidence of a radial metallicity gradient in Eri IV that would support this idea. The feature may also be a subsatellite of Eri IV (i.e., satellite of a UFD), which is predicted by Λ CDM (e.g., J. S. Bullock & M. Boylan-Kolchin 2017). However, given that there is no observational evidence of UFD satellites or field star capture, we favor the tidal disruption or stellar halo scenarios. That said, we do not have sufficient evidence to pin down the exact nature of Eri IV’s extended feature.

5. Summary and Conclusion

We present deep Magellan + Megacam photometric observations of two MW satellites: Cen I and Eri IV. These UFDs were recently discovered in the DELVE survey and observed spectroscopically by M. E. Heiger et al. (2024). Our data probe $\sim 2\text{--}3$ mag deeper than the discovery data, allowing us to derive robust distance measurements, constrain the structural properties and luminosities, and find a handful of potential new member stars. We construct high-quality morphological maps and perform extensive searches for extended structures to assess the dynamical state and nature of these systems. We find

that Cen I does not have a tidal feature associated with it, but Eri IV hosts an extended feature with multiple interpretations.

These deep data confirm that Cen I aligns well with the discovery observations in terms of its distance, structural parameters, and luminosity. We find six potential new member stars based on Gaia proper motions. For Eri IV, our data reveal it to be slightly closer ($D = 69.9 \pm 3.6$ kpc), more round ($\epsilon = 0.26 \pm 0.09$), and also dimmer, at $M_V = -3.55 \pm 0.24$ mag. Aside from these differences, our measurements for Eri IV are consistent with the discovery data in the following parameters: α_{2000} , δ_{2000} , r_h , and position angle. There are 14 potential new member stars based on Gaia proper motions. Both systems occupy a space on the size–luminosity plane consistent with other confirmed UFDs.

Our work helps to clear up some of the open questions surrounding the discovery photometry and the spectroscopic data: both Cen I and Eri IV exhibited hints of extended features in the discovery data, but spectroscopic analysis suggested that these overdensities were not the result of tidal disruption. Our photometry shows no compelling evidence that Cen I is disrupting. Eri IV, on the other hand, hosts an extended structure to the northeast of its central body (Figure 2). This structure may be the result of tidal disruption in the recent past, although we cannot rule out the possibility that this region arose from a merger or is a satellite itself. It seems as though Eri IV will remain an interesting UFD moving forward; the true nature of the extended structure may be understood through a combination of deeper and wider-field imaging data and detailed dynamical modeling. This work highlights the importance of deep imaging in conjunction with spectroscopy to specifically explore the extended structures, ultimately aiding in the understanding of the true nature of ultrafaint satellites.

Acknowledgments

We thank the anonymous reviewer, whose comments and suggestions improved the content of this paper. Q.O.C. acknowledges support from the Dartmouth Fellowship. D.J.S. and the Arizona team acknowledge support from NSF grant AST-2205863. Q.O.C. thanks Ryan Hickox and Elisabeth Newton for useful discussions.

This paper includes data gathered with the 6.5 m Magellan Telescope located at Las Campanas Observatory, Chile.

The DECam Local Volume Exploration Survey (DELVE; NOAO Proposal ID 2019A-0305; PI: Drlica-Wagner) is partially supported by Fermilab LDRD project L2019-011 and the NASA Fermi Guest Investigator Program Cycle 9 No. 91201. This project used data obtained with the Dark Energy Camera (DECam), which was constructed by the Dark Energy Survey (DES) collaboration. Funding for the DES Projects has been provided by the US Department of Energy, the US National Science Foundation, the Ministry of Science and Education of Spain, the Science and Technology Facilities Council of the United Kingdom, the Higher Education Funding Council for England, the National Center for Supercomputing Applications at the University of Illinois at Urbana-Champaign, the Kavli Institute of Cosmological Physics at the University of Chicago, the Center for Cosmology and Astro-Particle Physics at The Ohio State University, the Mitchell Institute for Fundamental Physics and Astronomy at Texas A&M University, Financiadora de Estudos e Projetos, Fundação Carlos Chagas Filho de Amparo à Pesquisa do Estado do Rio de












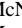
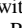
Janeiro, Conselho Nacional de Desenvolvimento Científico e Tecnológico and the Ministério da Ciência, Tecnologia e Inovação, the Deutsche Forschungsgemeinschaft, and the Collaborating Institutions in the Dark Energy Survey. The Collaborating Institutions are Argonne National Laboratory, the University of California at Santa Cruz, the University of Cambridge, Centro de Investigaciones Energéticas, Medioambientales y Tecnológicas-Madrid, the University of Chicago, University College London, the DES-Brazil Consortium, the University of Edinburgh, the Eidgenössische Technische Hochschule (ETH) Zürich, Fermi National Accelerator Laboratory, the University of Illinois at Urbana-Champaign, the Institut de Ciències de l'Espai (IEEC/CSIC), the Institut de Física d'Altes Energies, Lawrence Berkeley National Laboratory, the Ludwig-Maximilians Universität München and the associated Excellence Cluster Universe, the University of Michigan, the National Optical Astronomy Observatory, the University of Nottingham, The Ohio State University, the OzDES Membership Consortium, the University of Pennsylvania, the University of Portsmouth, SLAC National Accelerator Laboratory, Stanford University, the University of Sussex, and Texas A&M University. Based in part on observations at Cerro Tololo Inter-American Observatory, National Optical Astronomy Observatory, which is operated by the Association of Universities for Research in Astronomy (AURA) under a cooperative agreement with the National Science Foundation. Database access and other data services are hosted by the Astro Data Lab at the Community Science and Data Center (CSDC) of the National Science Foundation's National Optical Infrared Astronomy Research Laboratory, operated by the Association of Universities for Research in Astronomy (AURA) under a cooperative agreement with the National Science Foundation.



This work has made use of data from the European Space Agency (ESA) mission Gaia (<https://www.cosmos.esa.int/gaia>), processed by the Gaia Data Processing and Analysis Consortium (DPAC, <https://www.cosmos.esa.int/web/gaia/dpac/consortium>). Funding for the DPAC has been provided by national institutions, in particular the institutions participating in the Gaia Multilateral Agreement.

Facilities: Magellan:Clay, Gaia.

Software: IDL astronomy users library (W. B. Landsman 1993), SExtractor (E. Bertin & S. Arnouts 1996), numpy (C. R. Harris et al. 2020), pandas (J. Reback et al. 2021), astropy (Astropy Collaboration et al. 2022), Topcat (M. B. Taylor 2005).

ORCID iDs

Quinn O. Casey  <https://orcid.org/0009-0005-9002-4800>
 Burçin Mutlu-Pakdil  <https://orcid.org/0000-0001-9649-4815>
 David J. Sand  <https://orcid.org/0000-0003-4102-380X>
 Andrew B. Pace  <https://orcid.org/0000-0002-6021-8760>
 Denija Crnojević  <https://orcid.org/0000-0002-1763-4128>
 Amandine Doliva-Dolinsky  <https://orcid.org/0000-0001-9775-9029>
 William Cerny  <https://orcid.org/0000-0003-1697-7062>
 Mairead E. Heiger  <https://orcid.org/0000-0002-2446-8332>
 Alex H. Riley  <https://orcid.org/0000-0001-5805-5766>
 Alexander P. Ji  <https://orcid.org/0000-0002-4863-8842>
 Guilherme Limberg  <https://orcid.org/0000-0002-9269-8287>
 Laurella Marin  <https://orcid.org/0009-0008-3389-9848>
 Clara E. Martínez-Vázquez  <https://orcid.org/0000-0002-9144-7726>

Gustavo E. Medina  <https://orcid.org/0000-0003-0105-9576>
 Ting S. Li  <https://orcid.org/0000-0002-9110-6163>
 Sasha N. Campana  <https://orcid.org/0009-0007-9488-7050>
 Astha Chaturvedi  <https://orcid.org/0000-0001-5143-1255>
 Joanna D. Sakowska  <https://orcid.org/0000-0002-1594-1466>
 Alfredo Zenteno  <https://orcid.org/0000-0001-6455-9135>
 Julio A. Carballo-Bello  <https://orcid.org/0000-0002-3690-105X>
 Mahdieh Navabi  <https://orcid.org/0000-0001-9438-5228>
 Clecio R. Bom  <https://orcid.org/0000-0003-4383-2969>

References

- Astropy Collaboration, Price-Whelan, A. M., Lim, P. L., et al. 2022, *ApJ*, **935**, 167
- Bechtol, K., Drlica-Wagner, A., Balbinot, E., et al. 2015, *ApJ*, **807**, 50
- Belokurov, V., Walker, M. G., Evans, N. W., et al. 2010, *ApJL*, **712**, L103
- Belokurov, V., Zucker, D. B., Evans, N. W., et al. 2007, *ApJ*, **654**, 897
- Bernard, E. J., Ferguson, A. M. N., Schlafly, E. F., et al. 2014, *MNRAS*, **442**, 2999
- Bertin, E., & Arnouts, S. 1996, *A&AS*, **117**, 393
- Bertin, E., Mellier, Y., Radovich, M., et al. 2002, in ASP Conf. Ser. 281, *Astronomical Data Analysis Software and Systems XI* (San Francisco, CA: ASP), 228
- Binney, J., & Tremaine, S. 2008, in *Galactic Dynamics: Second Edition*, ed. J. Binney & S. Tremaine (Princeton, NJ: Princeton Univ. Press), 2008
- Bressan, A., Marigo, P., Girardi, L., et al. 2012, *MNRAS*, **427**, 127
- Bullock, J. S., & Boylan-Kolchin, M. 2017, *ARA&A*, **55**, 343
- Cantu, S. A., Pace, A. B., Marshall, J., et al. 2021, *ApJ*, **916**, 81
- Carlin, J. L., Sand, D. J., Muñoz, R. R., et al. 2017, *AJ*, **154**, 267
- Cerny, W., Chiti, A., Geha, M., et al. 2025, *ApJ*, **979**, 164
- Cerny, W., Drlica-Wagner, A., Li, T. S., et al. 2023a, *ApJL*, **953**, L21
- Cerny, W., Martínez-Vázquez, C. E., Drlica-Wagner, A., et al. 2023b, *ApJ*, **953**, 1
- Cerny, W., Pace, A. B., Drlica-Wagner, A., et al. 2021, *ApJL*, **920**, L44
- Cerny, W., Simon, J. D., Li, T. S., et al. 2023c, *ApJ*, **942**, 111
- Chiti, A., Frebel, A., Simon, J. D., et al. 2021, *NatAs*, **5**, 392
- Choi, Y., Nidever, D. L., Olsen, K., et al. 2018, *ApJ*, **869**, 125
- Crnojević, D., Sand, D. J., Zaritsky, D., et al. 2016, *ApJL*, **824**, L14
- Drlica-Wagner, A., Bechtol, K., Allam, S., et al. 2016, *ApJL*, **833**, L5
- Drlica-Wagner, A., Bechtol, K., Rykoff, E. S., et al. 2015, *ApJ*, **813**, 109
- Drlica-Wagner, A., Ferguson, P. S., Adamów, M., et al. 2022, *ApJS*, **261**, 38
- Dotter, A., Chaboyer, B., Jevremović, D., et al. 2008, *ApJS*, **178**, 89
- Eyer, L., Audard, M., Holl, B., et al. 2023, *A&A*, **674**, A13
- Gaia Collaboration, Brown, A. G. A., Vallenari, A., et al. 2021, *A&A*, **649**, A1
- Gaia Collaboration, Prusti, T., de Bruijne, J. H. J., et al. 2016, *A&A*, **595**, A1
- González-Morales, A. X., Marsh, D. J. E., Peñarrubia, J., et al. 2017, *MNRAS*, **472**, 1346
- Harris, C. R., Millman, K. J., van der Walt, S. J., et al. 2020, *Natur*, **585**, 357
- Harris, W. E. 2010, arXiv:1012.3224
- Heiger, M. E., Li, T. S., Pace, A. B., et al. 2024, *ApJ*, **961**, 234
- Homma, D., Chiba, M., Komiyama, Y., et al. 2019, *PASJ*, **71**, 94
- Homma, D., Chiba, M., Komiyama, Y., et al. 2024, *PASJ*, **76**, 733
- Homma, D., Chiba, M., Okamoto, S., et al. 2018, *PASJ*, **70**, S18
- Ji, A. P., Kposov, S. E., Li, T. S., et al. 2021, *ApJ*, **921**, 32
- Kim, D., & Jerjen, H. 2015, *ApJL*, **808**, L39
- Kposov, S. E., Belokurov, V., Torrealba, G., et al. 2015, *ApJ*, **805**, 130
- Kposov, S. E., Walker, M. G., Belokurov, V., et al. 2018, *MNRAS*, **479**, 5343
- Landsman, W. B. 1993, in ASP Conf. Ser. 52, *Astronomical Data Analysis Software and Systems II* (San Francisco, CA: ASP), 246
- Martin, N. F., de Jong, J. T. A., & Rix, H.-W. 2008, *ApJ*, **684**, 1075
- Martin, N. F., Ibata, R. A., Lewis, G. F., et al. 2016, *ApJ*, **833**, 167
- Martin, N. F., Nidever, D. L., Besla, G., et al. 2015, *ApJL*, **804**, L5
- Martínez-Vázquez, C. E., Cerny, W., Vivas, A. K., et al. 2021, *AJ*, **162**, 253
- Martínez-Vázquez, C. E., Vivas, A. K., Gurevich, M., et al. 2019, *MNRAS*, **490**, 2183
- Mau, S., Cerny, W., Pace, A. B., et al. 2020, *ApJ*, **890**, 136
- Mau, S., Drlica-Wagner, A., Bechtol, K., et al. 2019, *ApJ*, **875**, 154
- McConnachie, A. W. 2012, *AJ*, **144**, 4
- McLeod, B., Geary, J., Conroy, M., et al. 2015, *PASP*, **127**, 366
- McNanna, M., Bechtol, K., Mau, S., et al. 2024, *ApJ*, **961**, 126
- Moskowitz, A. G., & Walker, M. G. 2020, *ApJ*, **892**, 27
- Muñoz, R. R., Côté, P., Santana, F. A., et al. 2018, *ApJ*, **860**, 66
- Muñoz, R. R., Geha, M., & Willman, B. 2010, *AJ*, **140**, 138
- Muñoz, R. R., Majewski, S. R., & Johnston, K. V. 2008, *ApJ*, **679**, 346

- Mutlu-Pakdil, B., Sand, D. J., Carlin, J. L., et al. 2018, *ApJ*, **863**, 25
- Mutlu-Pakdil, B., Sand, D. J., Crnojević, D., et al. 2020, *ApJ*, **902**, 106
- Ou, X., Chiti, A., Shipp, N., et al. 2024, *ApJ*, **966**, 33
- Pace, A. B. 2024, arXiv:2411.07424
- Pace, A. B., Erkal, D., & Li, T. S. 2022, *ApJ*, **940**, 136
- Pace, A. B., & Li, T. S. 2019, *ApJ*, **875**, 77
- Peñarrubia, J., Errani, R., Walker, M. G., et al. 2024, *MNRAS*, **533**, 3263
- Pietrinferni, A., Cassisi, S., Salaris, M., et al. 2004, *ApJ*, **612**, 168
- Querci, L., Pallottini, A., Branca, L., et al. 2025, *A&A*, **694**, A17
- Reback, J., Jbrockmendel, McKinney, W., et al. 2021, pandas-dev/pandas: Pandas 1.3.5, Zenodo, doi:10.5281/zenodo.5774815
- Rhode, K. L., Smith, N. J., Crnojevic, D., et al. 2023, *AJ*, **166**, 180
- Richstein, H., Patel, E., Kallivayalil, N., et al. 2022, *ApJ*, **933**, 217
- Riley, A. H., Shipp, N., Simpson, C. M., et al. 2024, arXiv:2410.09144
- Rockosi, C. M., Odenkirchen, M., Grebel, E. K., et al. 2002, *AJ*, **124**, 349
- Safarzadeh, M., & Spergel, D. N. 2020, *ApJ*, **893**, 21
- Salpeter, E. E. 1955, *ApJ*, **121**, 161
- Sand, D. J., Olszewski, E. W., Willman, B., et al. 2009, *ApJ*, **704**, 898
- Sand, D. J., Seth, A., Olszewski, E. W., et al. 2010, *ApJ*, **718**, 530
- Sand, D. J., Strader, J., Willman, B., et al. 2012, *ApJ*, **756**, 79
- Schlegel, D. J., Finkbeiner, D. P., & Davis, M. 1998, *ApJ*, **500**, 525
- Shipp, N., Drlica-Wagner, A., Balbinot, E., et al. 2018, *ApJ*, **862**, 114
- Shipp, N., Panithanpaisal, N., Necib, L., et al. 2023, *ApJ*, **949**, 44
- Shipp, N., Riley, A. H., Simpson, C. M., et al. 2024, arXiv:2410.09143
- Simon, J. D. 2019, *ARA&A*, **57**, 375
- Simon, J. D., Li, T. S., Erkal, D., et al. 2020, *ApJ*, **892**, 137
- Smith, S. E. T., Jensen, J., Roediger, J., et al. 2023, *AJ*, **166**, 76
- Stetson, P. B. 1994, *PASP*, **106**, 250
- Strigari, L. E. 2018, *RPPh*, **81**, 056901
- Tan, C. Y., Cerny, W., & Drlica-Wagner, A. 2025, *ApJ*, **979**, 176
- Tarumi, Y., Yoshida, N., & Frebel, A. 2021, *ApJL*, **914**, L10
- Taylor, M. B. 2005, in ASP Conf. Ser. 347, Astronomical Data Analysis Software and Systems XIV (San Francisco, CA: ASP), 29
- Tollerud, E. J., Beaton, R. L., Geha, M. C., et al. 2012, *ApJ*, **752**, 45
- Torrealba, G., Belokurov, V., Koposov, S. E., et al. 2018, *MNRAS*, **475**, 5085
- Torrealba, G., Koposov, S. E., Belokurov, V., et al. 2016a, *MNRAS*, **459**, 2370
- Torrealba, G., Koposov, S. E., Belokurov, V., et al. 2016b, *MNRAS*, **463**, 712
- Vivas, A. K., Walker, A. R., Martínez-Vázquez, C. E., et al. 2020, *MNRAS*, **492**, 1061
- Walsh, S. M., Willman, B., Sand, D., et al. 2008, *ApJ*, **688**, 245
- Wang, M. Y., de Boer, T., Pieres, A., et al. 2019, *ApJ*, **881**, 118
- Weinberg, D. H., Bullock, J. S., Governato, F., et al. 2015, *PNAS*, **112**, 12249
- Wetzel, A. R., Hopkins, P. F., Kim, J.-hoon, et al. 2016, *ApJL*, **827**, L23
- Zucker, D. B., Belokurov, V., Evans, N. W., et al. 2006, *ApJL*, **650**, L41